HOKKAIDO UNIVERSITY

Instructions for use

Anisotropic defect distribution in He⁺-irradiated 4H-SiC: effect of stress on defect distribution

Subing Yang, Yuki Nakagawa, Minako Kondo, Tamaki Shibayama[*]

Faculty of Engineering, Hokkaido University, Sapporo, Hokkaido 060-8628, Japan

* Corresponding author.

E-mail address: shiba@qe.eng.hokudai.ac.jp

Abstract

Irradiation-induced anisotropic swelling in hexagonal α-SiC is known to degrade the mechanical properties of SiC; however, the associated physical mechanism and microstructural process remain insufficiently understood. In this study, an anisotropic swelling condition where the surface normal direction was allowed to freely expand with constraint in the lateral direction was introduced in 4H-SiC using selected-area He$^+$ irradiation, and the internal defect distribution was investigated using transmission electron microscopy (TEM) and advanced scanning TEM. The defect distribution was compared to that in non-selected-area He$^+$-irradiated 4H-SiC and electron-irradiated TEM-foil 4H-SiC. An anisotropic defect distribution was observed in the selected-area He$^+$-ion-irradiated 4H-SiC, with interstitial defects preferentially redistributed in the surface normal direction ([0004]) and negative volume defects (such as vacancies and/or carbon antisite defects) dominantly located in the lateral directions ([11$\bar{2}$0] and [10$\bar{1}$0]). This anisotropy of the defect distribution was substantially lower in the non-selected-area He$^+$-irradiated and electron-irradiated samples. The stress condition in the three samples was also measured and analyzed. In the selected-area He$^+$-irradiated 4H-SiC, compressive stress was introduced in the lateral directions (([10$\bar{1}$0] and [11$\bar{2}$0])), with little stress introduced in the surface normal direction ([0004]); this stress condition was introduced at the beginning of ion irradiation. The compressive stress likely inhibits the formation of interstitial defects in the lateral directions, enhancing the anisotropy of the defect distribution in

SiC.

1. Introduction

Because of its excellent mechanical, structural, and electronic properties, silicon carbide (SiC) has been proposed as an excellent candidate for various nuclear, aerospace, and electronic applications [1-4]. SiC is exposed to various types of irradiation during the fabrication of electronic devices (such as ion implantation for doping carriers) or when applied in nuclear or aerospace environments (neutron or other high-energy particle irradiations) [5-6]. This irradiation inevitably introduces damage, which greatly affects the mechanical and electronic properties. Particular interest has been focused on irradiation-induced dimension instability, including swelling [7] and creeping [8], which is a key issue for long-term structural performance in nuclear reactors. In order to resolve these issues, one of the key challenges is to simulate the various damages introduced by neutron irradiation. Neutron irradiation could induce a displacement cascade of lattice atoms, and various defects would form with diffusion and combination of the displaced lattice atoms. However, currently neutron irradiation experiments are hampered by long time, expensive cost and high radioactivity [9]. High energy electron irradiation could also induce displacement of lattice atoms that it can be used to simulate the irradiation damage. Although it has a higher irradiation flux and damage rates, it cannot cause the displacement cascade. Also, its penetration depth is thin,

3

and it is usually performed on the foil sample. To some extent, energetic ion irradiation is a promising simulation method, which not only could induce the displacement cascade of lattice atoms, but also has the advantages of high damage rates, minimal residual radio activity and low cost [9]. The application of modern materials modeling methods has also made great progress to study radiation effects on SiC. Y. Katoh et al. [10] has reported the recent advances and outstanding challenges in modeling of radiation induced defects and their interactions with microstructure, transport of fission products through SiC, and thermomechanical properties of SiC, which shows that such modeling can be powerful for the design of SiC-based materials for the harsh environments encountered in fission and fusion applications. Using first-principles density functional theory calculations, N. Daghbouj et al. [11] advanced the understanding of the mechanism of the bubble-to-platelet transition in the He^+-irradiated 6H-SiC. Due to the small size of defect clusters (such as < 1 nm) that they are difficult to measure in traditional TEM, hence, how to measure and quantify their distribution is an outstanding challenge. Recently, C. Liu, I. Szlufarska and their coworker [7] developed a cluster dynamics model that can describe the evolution of irradiation-induced defects, and this mode closes the gap between simulation and experimental results in terms of the cluster size distribution.

In the previously reported studies, sufficient effort has been dedicated to investigating the irradiation-induced swelling in SiC. S. Leclerc et al. has reported swelling of He^+-irradiated 4H-SiC at different fluences, different

irradiation temperature [12] and different annealing temperature [13]. They have well characterized swelling, disorder and defects evolution in irradiated SiC, moreover, the contribution of different types of defects or damage to swelling was also classified. The disordering behavior, up to amorphization, of both irradiated 6H-SiC and 3C-SiC polytypes was successfully characterized and modelled by A. Debelle et al. [14], and the simulation results were consistent with the experimental results. In these reported results, most investigations were focused on the irradiation-induced isotropic swelling. However, apart from conventional isotropic swelling, irradiation may induce anisotropic swelling in hexagonal-crystal α-SiC [15], which has also been observed in many other hexagonal-crystal ceramic materials including aluminum nitride [16], silicon nitride [17], titanium aluminum carbide [18], and titanium silicon carbide [19]. Besides, it has also been reported that the thermal expansion coefficients of α_{11} is 3.21×10^{-6}, 5.6×10^{-6} and 12.9×10^{-6} (1/°C) for 4H-SiC [20], AlN [21], and Cr2GeC [22], but α_{33} is 3.09×10^{-6}, 6.9×10^{-6}, 17.6×10^{-6} (1/ °C), respectively. Up to now, the irradiation-induced anisotropic swelling in α-SiC was still insufficient. Compared with isotropic swelling, anisotropic swelling is more deleterious in terms of the resulting degradation of mechanical properties. The swelling itself is not considered a key limitation for the application of SiC in nuclear reactors; however, the significant internal stress induced by differential swelling can lead to degradation of the component structures [18,23,24]. Moreover, fractures or microcracks have also been reported to preferentially occur at the grain

5

boundaries in materials with such anisotropic swelling [18,19]. It appears reasonable that α-SiC and other ceramics with a hexagonal crystal structure may display differing irradiation-induced expansion in different directions, leading to loss of the original crystal integrity and degradation of the mechanical properties. However, α-SiC can also exhibit isotropic swelling. For example, L.L. Snead et al. reported an essentially equivalent dilation of the <a> and <c> axes for neutron-irradiated α-6H-SiC near 60 °C [25]. In addition, Y. Lin and coworkers also observed anisotropic crystal swelling in Si^{2+}-irradiated cubic-β-3C SiC at 1000 °C [26]. Furthermore, the variation of swelling behavior for both α- and β-SiC resulting from different irradiation conditions (different irradiation particles, doses, and temperatures) [25,27,28] complicates the understanding of anisotropic swelling in SiC. To date, the underlying mechanism of this anisotropic swelling remains far from well understood in terms of the physical mechanism and microstructural process.

According to the correlation of defects with swelling, with volumetric swelling dominated by various defects, especially point defects or tiny defect clusters at room temperature [7,29], it is reasonable to consider that anisotropic swelling should be correlated to the defect distribution for different crystal orientations. Various attempts have been made to explore the defect distribution and disorder accumulation in irradiated α-SiC. Jiang et al. observed anisotropic lattice expansion in H^+-implanted α-6H-SiC at extremely low doses below 340 K. In that study, the anisotropic swelling was mainly attributed to irradiation-induced vacancies in the basal plane

based on a theoretical analysis [27]. However, the defect distribution in the samples was not provided. Zhang et al. [30] observed an anisotropy of disorder accumulation in Au$^+$-irradiated α-4H-SiC at 165 K using Rutherford backscattering spectroscopy, which was well explained by the stable defect configuration with most interstitial configurations parallel to the [0001] direction according to the molecular dynamic simulation. However, it is not clear that this anisotropic disorder accumulation occurs for anisotropic or isotropic swelling in SiC. Therefore, to obtain insight into the anisotropic swelling mechanism, a fundamental understanding of the detailed defect distribution for different orientations or planes in SiC with anisotropic swelling is needed. However, the defect distribution in α-SiC with anisotropic swelling has rarely been reported because of the relatively small size of the defects, which are difficult to observe using conventional transmission electron microscopy (TEM), especially at relatively low irradiation temperature [7].

Kondo et al. [31] explored the stable surface class in 6H-SiC by analyzing nano-void shapes using TEM, which suggests that the observation of some second-type defects formed by the accumulation of point defects might provide insight into the defect distribution in irradiated α-SiC. In addition, in our previous study, anisotropic swelling or strain was introduced in 4H-SiC using selected-area ion irradiation, as demonstrated by atomic force microscopy and electron back scattering diffraction (EBSD) [32]. Hence, this approach might be useful to explore the phenomenon and underlying mechanism of anisotropic swelling in SiC. In

165 the current study, anisotropic swelling was introduced in 4H-SiC using

166 selected-area ion irradiation, and the defect distribution in different

167 directions was explored using various TEM techniques. An anisotropic

168 defect distribution was observed in the irradiated 4H-SiC. In addition, the

169 potential mechanism for this defect distribution is discussed.

170 **2. Experimental procedures**

171 Single-crystalline n-type 4H-SiC (0001) substrates (Xiamen Powerway

172 Advanced Material Co., Ltd., Xiamen, China) with dimensions of 10×10

173 $\times$ 0.33 mm^3 were irradiated with 100-keV He$^+$ at room temperature to

174 fluences of 1×10^{15} and 5×10^{16} cm^{-2}. During irradiation, the irradiation flux

175 was kept at a level of 6.2×10^{12} He·cm^{-2}·s^{-1}, and the beam raster scanning

176 was performed to reach a homogeneous irradiation condition in the

177 irradiated area.

178 For comparison, both selected-area irradiation and non-selected-area

179 irradiation were performed. During selected-area irradiation, part of the

180 sample was covered by a mask with a hole 8 mm in diameter to clearly

181 distinguish between the irradiated and unirradiated areas. More details of

182 the selected-area ion irradiation procedure are provided in Ref. [32]. The

183 non-selected-area irradiation, i.e., without using the mask, was also

184 prepared at room temperature with a fluence of 5×10^{16} cm^{-2}. The damage

185 and injected helium profile for He$^+$ into SiC were calculated using SRIM

186 2013 in full-cascade mode. The sample density and threshold displacement

187 energy for the C and Si sub-lattices used in the calculation were 3.21

188 g·cm^{-3} and 21 and 35 eV [33], respectively. The total penetration depth

8

predicted by simulation was approximately 600 nm, and the highest damage was predicted to occur at approximately 450 nm with a dose of about 4.2 dpa (displacement per atom, dpa) for the fluence of 5×10^{16} cm^{-2} [34]. In addition, a peak helium concentration of about 2.95% is observed at about 470 nm in depth.

After irradiation, cross-sectional thin foils for TEM were prepared from irradiated areas using gallium ions in a focused-ion-beam system (JEOL, JEM-90320FIB). The ion accelerating voltage was 30 kV, and the samples were thinned to a final thickness of about 100 nm. To minimize the damage introduced into the TEM samples by gallium ions during FIB, these TEM samples were then polished by lower energy Ar ions using GentleMill (TECHNOORG-lINDA ltd. Co., Gentle Mill IV8 HI). Both sides of TEM samples were polished with a 1.5 kV beam at 8º incident angle for 40 mins, then 0.5 kV at 15º for 30 mins. The microstructural features of the irradiated 4H-SiC were observed using TEM (JEOL, JEM-2000FX) at an operation voltage of 200 kV. The average size and number density of defects were counted and calculated from weak-beam dark-field TEM images, with 3–5 images used for each calculation. The TEM images used for damage counting are all taken at the same magnification, then adjusted to the same background contrast and brightness using Gatan DigitalMicrograph. The BSDs were then marked by Adobe Photoshop based on the contrast difference from the background, which could be automatically counted using the software of MAC-View Version.4 (Mountech Co., Ltd.). The average size of a BSD was recorded by the

Heywood diameter. The thicknesses of the observation regions were measured using electron energy loss spectroscopy (EELS) with a Cs-corrected scanning transmission electron microscope (FEI, Titan G2 60-300). High-resolution TEM (HR-TEM) analysis, high-angle annular dark field (HAADF) and annular bright field (ABF) scanning transmission electron microscopy (STEM), and core-loss EELS studies were also performed using the Cs-corrected STEM. The operation voltage was 300 kV. HAADF- and ABF-STEM images were simultaneously obtained with a 17.8-mrad semi-convergence angle and 50–200 and 10.36–24.48 mrad collection angles for the HAADF and ABF mode, respectively.

Together with the strain, the elastic stress in the irradiated area was also determined using EBSD and Crosscourt3 software with the elasticity coefficients of 4H-SiC. A field-emission scanning electron microscope (JEOL JSM–7001FA) equipped with an EBSD detector was used to obtain EBSD patterns, operating at an acceleration voltage of 20 kV, a sample tilt of 70°, and a scan size and scan step of 20×20 μm^2 and 0.1 μm, respectively. The elasticity coefficients provided by the Crosscourt3 software, C11=501 GPa, C12=111 GPa, C13=52 GPa, C22=501 GPa, C33=553 GPa, and C44=163 GPa, were consistent with previously reported results [35]. The stress was determined by analyzing the EBSD patterns using the CrossCourt3 software. Details of this strain/stress measurement method using EBSD and the strain results have been published elsewhere (Ref. [32]).

Electron irradiation of thin-foil 4H-SiC samples using a multi-beam

ultra-high voltage electron microscope (multi-beam HVEM, JEOL, JEM-ARM1300) was also performed. The TEM samples for electron irradiation were prepared from unirradiated areas of the selected-area He$^+$-irradiated 4H-SiC samples using FIB; before electron irradiation, the TEM samples were annealed at 600 °C for 30 min in the multi-beam HVEM to remove any potential internal stress. The electron irradiation was performed at room temperature at an accelerating voltage of 1.25 MV with an irradiation area diameter of approximately 2 μm. The electron flux was approximately 1.2×10^{24} e·m^{-2}·s^{-1}, and the total irradiation time was 1 h. During irradiation, the electron beam was controlled to be parallel to the [11$\bar{2}$0] orientation. After electron irradiation, the defect distribution in electron-irradiated thin-foil 4H-SiC samples was also characterized using 200-kV TEM (JEOL, JEM-2000FX).

3. Results

3.1 Microstructure in He$^+$-ion-irradiated 4H-SiC

After irradiation, the internal microstructure of the He$^+$-implanted 4H-SiC with a fluence of 5×10^{16} cm^{-2} was examined, as shown in Fig. 1(a) together with the simulated damage and He$^+$ distribution profiles obtained using SRIM 2013. Because of the different irradiation damage levels, three types of regions with distinct bright-field image contrast (gray, black, and white) are discernible in Fig. 1(a), denoted as the A, B, and C layer, respectively, with the B layer further separated into B$_1$ and B$_2$ layers. As indicated by the TEM image contrast and selected-area diffraction, the near-surface layer (A layer) with gray contrast contained only minimal damage and still

maintained good crystallinity (as observed in Fig. 1(b)). However, in the highest damage region, where the contrast was white (C layer), an amorphous state was confirmed by observation of the diffraction, as shown in Fig. 1(c). In addition, the two black layers (B_1 and B_2 layers) adjacent to the amorphous layer appear to contain significant defects.
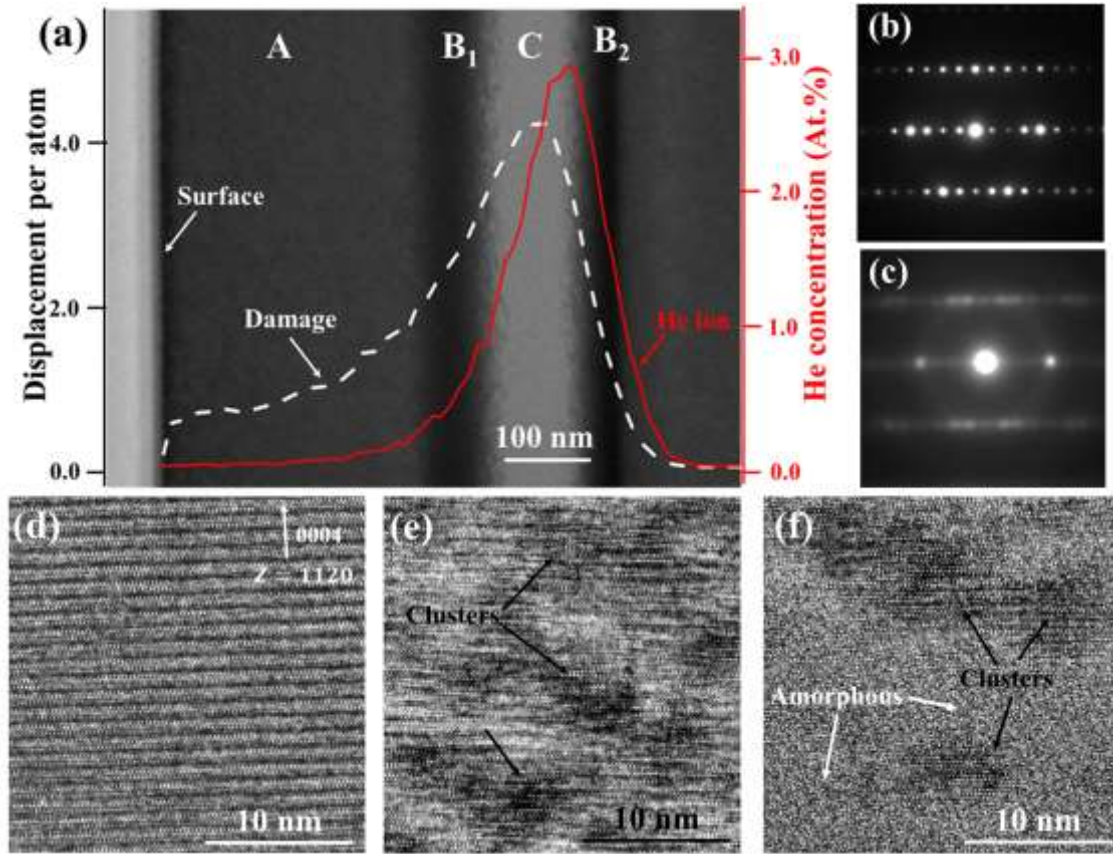

Fig. 1. Internal microstructure distribution of He$^+$-irradiated 4H-SiC up to a fluence of 5 × 10^{16} cm^{-2}. (a) Cross-sectional micrograph of He$^+$-implanted 4H-SiC and depth distribution of displacement damage (white dashed line) and He concentration (red solid line). (b, c) Diffraction patterns corresponding to the (b) A layer and (c) C layer. (d-f) High-resolution TEM images obtained from different regions: (d) A layer, (e) B_1 layer, and (f) near the interface between the B_1 and C layer. The images were taken near the $[11\bar{2}0]$ zone axis.

274

To resolve the defects in each region, HR-TEM images were obtained along the $[11\bar{2}0]$ zone axis, which are displayed in Fig. 1(d-f), with Fig. 1(d), 1(e), and 1(f) corresponding to the A layer, B_1 layer, and the interface between the B_1 and C layer (amorphous/crystal interface), respectively. In the A layer, the basal plane structure was maintained, which agrees well with the diffraction analysis shown in Fig. 1(b). In addition, the contrast of a few defects can be observed in Fig. 1(d). The main defects in the surface region might be point defects or tiny defect clusters that are difficult to clearly distinguish using HR-TEM [28]. However, in the relatively high-damage region (B_1 layers), the crystal exhibited obvious disorder (Fig. 1(e)). Black spots are clearly observed in this image, which are so-called black spot defects (BSDs) [7,11,36], a type of point-defect clusters composed of vacancies and interstitials in irradiated SiC. A small fraction of these black spots may also correspond to small dislocation loops according to previously reported results [37]; however, here, we consider all of them to be BSDs for convenient discussion. Fig. 1(f) shows the microstructure near the amorphous/crystal interface; BSDs are also visible, and some even appear in the amorphous region like an island.

3.2 Defect distribution

The presence of lattice defects in crystalline materials leads the planes close to the defects to bend. Bending of the lattice planes results in a change of diffraction and therefore a change in the image contrast; information about the defects can thus be obtained by studying the contrast

13

298 in TEM [38]. To identify characteristics of the defect clusters (BSDs),

299 different reflections corresponding to different sets of lattice planes were

300 used to explore the defect distribution in selected-area He$^+$-irradiated

301 4H-SiC. The distributions of BSDs under different TEM two-beam

302 observation conditions are presented in Fig. 2, with Fig. 2(a, b) obtained at

303 diffraction vector g = [0004] and Fig. 2(c, d) obtained at g = [11$\bar{2}$0]. These

304 images were obtained from the same area, and for orientation, a mark was

305 made by focused-electron-beam irradiation using a JEM-2000FX (200 kV).

306 Under the two-beam observation condition, the BSDs were clearly

307 observed in both the bright-field and dark-field images as black spots (Fig.

308 2(a) and 2(c)) and white spots (Fig. 2(b) and 2(d)), respectively. Comparing

309 the images in Fig. 2(a) and (b) with those in Fig. 2(c) and (d), it is apparent

310 that more BSDs appeared in the [0004] direction (Fig. 2(a) and (b)) than in

311 the [11$\bar{2}$0] direction (Fig. 2(c) and (d)). Moreover, the defects observed

312 with the reflection vector of [0004] became invisible with the reflection

313 vector of [11$\bar{2}$0], marked by a white square, and vice versa (marked by a

314 red circle). The details of the lattice-plane bending generally depend on the

315 characteristic of the defect [38]. According to the $\boldsymbol{g} \cdot \boldsymbol{b} = 0$ invisible

316 criterion for planar defects [39-41], the defects observed in Fig. 2 should be

317 a type of planar defect that formed in the corresponding orientation or

318 plane. Similar results were also observed for the reflection vectors g =

319 [0004] and g = [10$\bar{1}$0] (Fig. S1 in supplementary material), with BSDs

320 observed in one direction becoming invisible in the other direction. Hence,

321 in these samples, the observed BSDs under different diffraction conditions

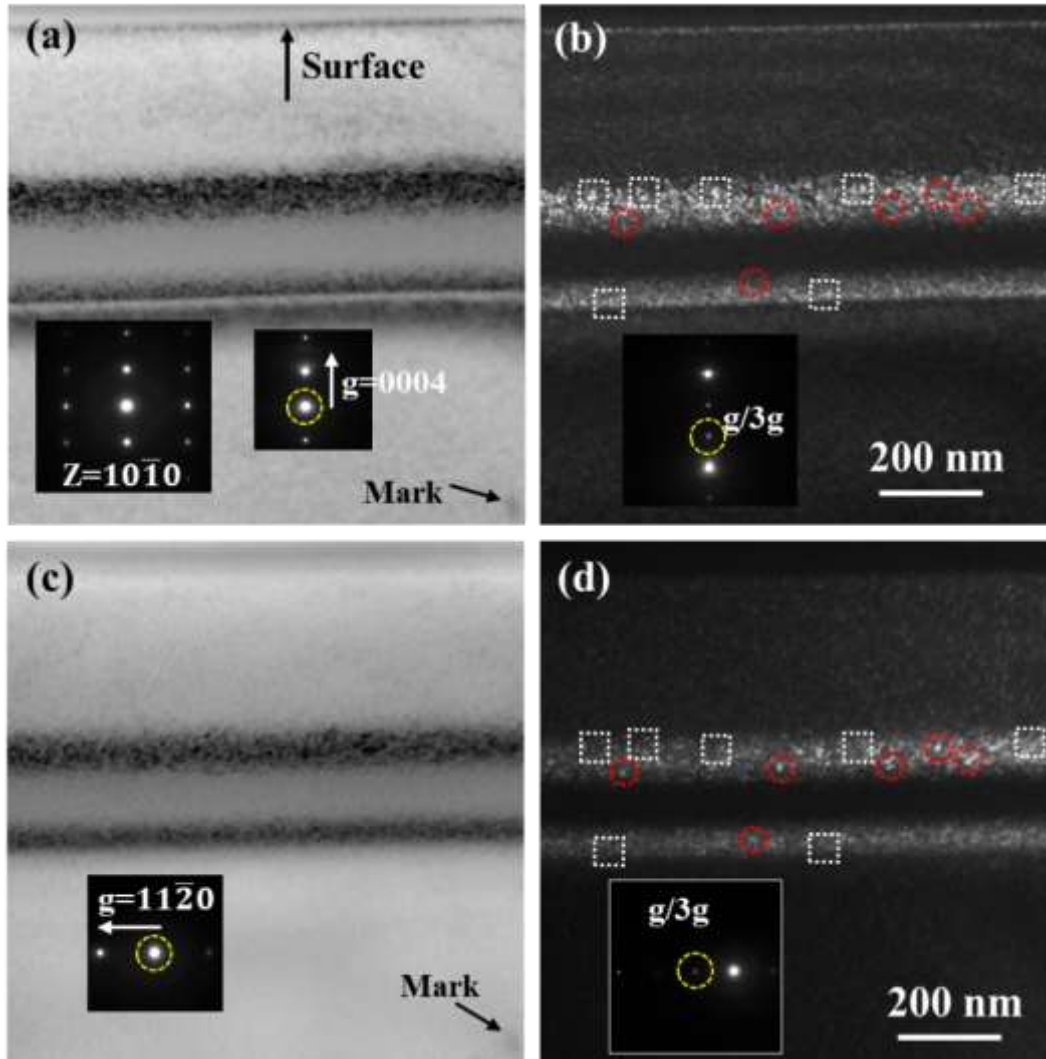322 appeared to be the plane defects formed in each reflecting plane.

323
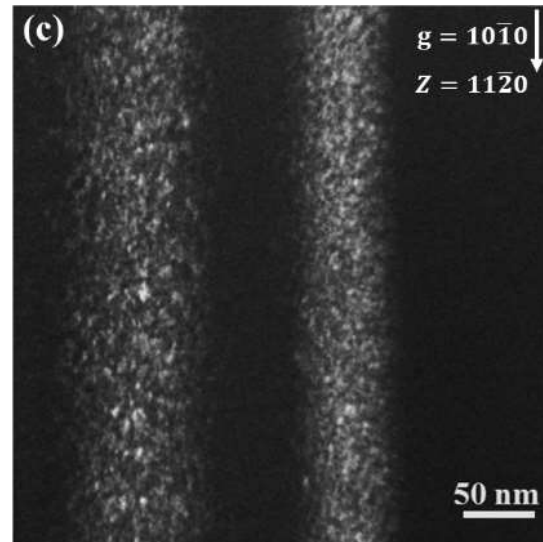
Fig. 2 TEM images of BSDs under different two-beam observation conditions: (a, b) g=0004 and (c, d) g=11$\bar{2}$0, with (a, c) bright-field images and (b, d) weak-beam dark-field images, g/3g. These images were obtained from the same area with a mark made for orientation purposes.

More detailed comparison of the defects formed in different orientations or planes was performed, as shown in Fig. 3. The images in Fig. 3(a)–(c) were obtained from the same area with Fig. 3(a) in the two-beam bright

field condition (diffraction condition g=0004) and Fig. 3(b) and 3(c) in different weak-beam dark-field conditions (g/3g, with g=0004 for (b) and g=10$\bar{1}$0 for (c)). The images in Fig. 3(d) and 4(e) were also obtained from the same area in different weak-beam dark-field conditions with g/3g and g=0004 for Fig. 3(d) and g=11$\bar{2}$0 for Fig. 3(e).
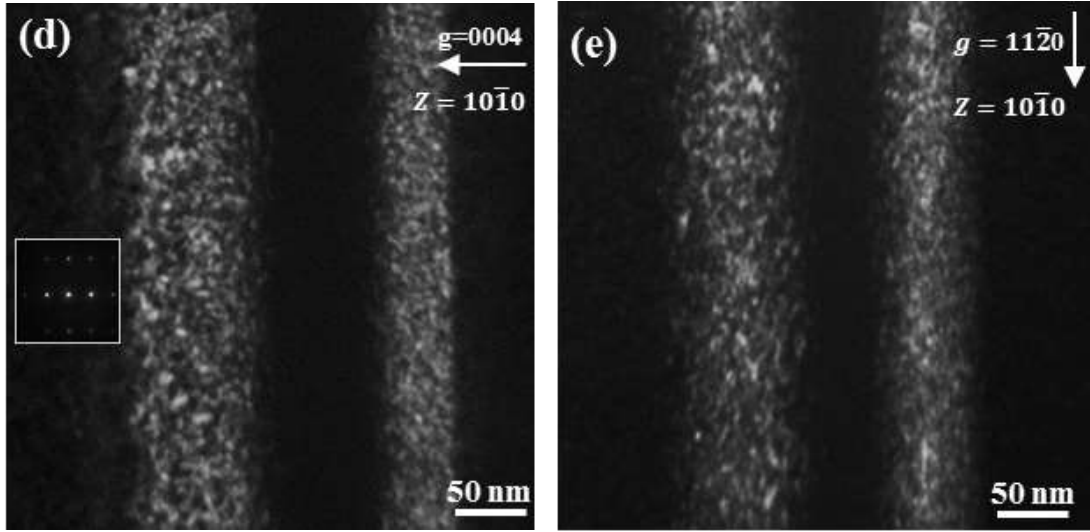
339
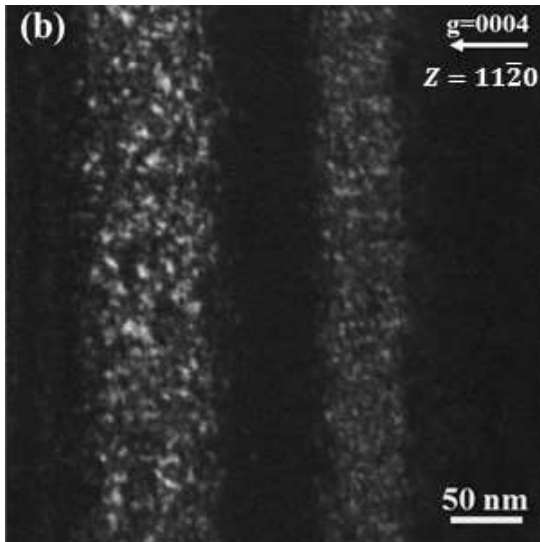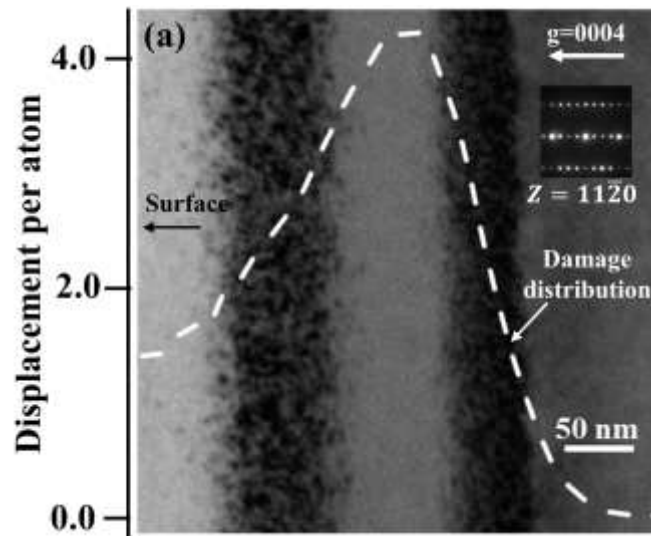
Fig. 3. TEM images of irradiated 4H-SiC taken under different observation conditions.
(a–c) were obtained from the same position: (a) two-beam bright-field image and (b, c)
g/3g weak-beam dark-field images with g=0004 for (b) and g=$10\bar{1}0$ for (c). (d, e) were
obtained from same position with g/3g weak-beam dark field and g=0004 for (d) and
g=$11\bar{2}0$ for (e).

These images show the different distributions of BSDs under different
diffraction conditions (g=0004, g=$10\bar{1}0$, and g=$11\bar{2}0$) in terms of the
defect size and number density. The average size and number density of
BSDs in region B_1 with different diffraction conditions were counted using
weak-beam dark-field images, and the results are summarized in Table 1.
The BSDs appearing in the [0004] direction had the highest number density
followed by those in the [$11\bar{2}0$] and [$10\bar{1}0$] directions, and the average
size of BSDs formed in the [0004] direction was also substantially larger
than that in the [$11\bar{2}0$] and [$10\bar{1}0$] directions. In Fig. 4(a), the BSD size
distribution profiles for the [$10\bar{1}0$], [$11\bar{2}0$], and [0004] directions greatly

17

356 differ. Although the peak of the profile of the [10$\bar{1}$0], [11$\bar{2}$0], and [0004]

357 directions occurred at approximately 4 nm, the number density of relatively

358 large-size BSDs (≥8 nm) was highest in the [0004] direction. In particular

359 for the [10$\bar{1}$0] profile, there was a lack of relatively large BSDs (≥8 nm).

360 These results suggest an anisotropic defect distribution in the selected-area

361 ion-irradiated 4H-SiC, and the anisotropy of the BSD distribution can be

362 summarized as more and larger BSDs preferentially forming in the [0004]

363 orientation compared with in the [10$\bar{1}$0] and [11$\bar{2}$0] orientations.

364 Table 1 Average size and number density of BSDs in different orientations.

365 The error bars represent the standard deviations

Conditions		11$\bar{2}$0	10$\bar{1}$0	0004
Selected-area ion irradiation	Average size (nm)	4.5 ±0.78	3.9 ±0.52	5.5 ±0.33
	Number density (10^{22} m^{-3})	1.6 ±0.15	1.1 ±0.18	2.9 ±0.28
Non-selected-area ion irradiation	Average size (nm)	4.7 ±0.35	5.0 ±0.58	4.7 ±0.52
	Number density (10^{22} m^{-3})	3.1 ±0.62	2.7 ±0.45	3.5 ±0.68
Electron irradiation	Average size (nm)		6.2 ±0.39	7.1 ±0.17
	Number density (10^{22} m^{-3})		0.72 ±0.018	1.1 ±0.015

366

367

368

369

370
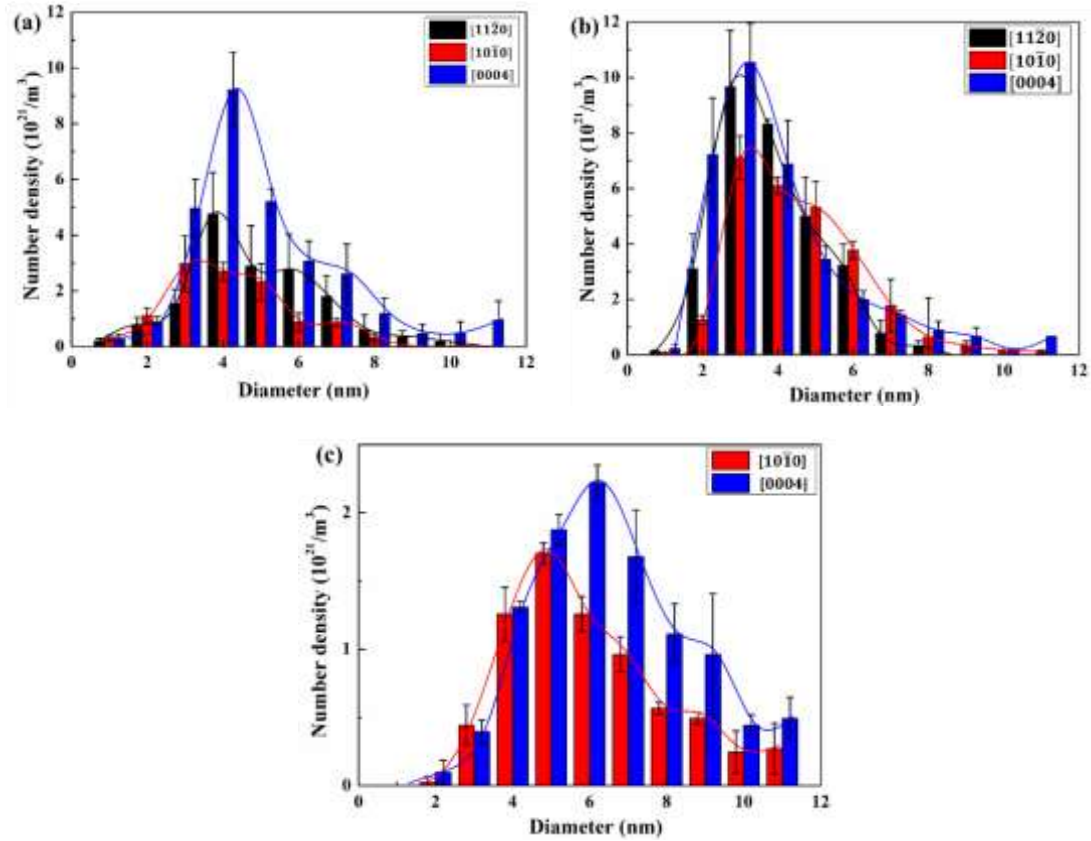
Fig. 4. Size distribution of BSDs in different orientations: (a) selected-area ion-irradiated sample, (b) non-selected-area ion-irradiated sample, and (c) electron-irradiated thin-film TEM sample. The error bars represent the standard deviations.

3.3 Nature of defect type

The nature of the irradiation-induced defect clusters was explored using ABF-STEM and HAADF-STEM. HAADF-STEM is a robust technique for identifying the position of atoms and atomic columns. When applied in a restricted zone-axis orientation, the contrast in a HAADF image is strongly dependent on the atomic number (Z^n, where n≈1.7) and the local thickness [42], which provides an approximate method for identifying atomic species.

ABF-STEM imaging can also be used to directly detect the position of atoms [43], providing a complementary contrast to HAADF, as shown in Fig. 5. For instance, the Si atom columns correspond to the black spots in the ABF-STEM images and the bright spots in the HAADF-STEM images.

The ABF- and HAADF-STEM images in Fig. 5(b) and (c) were obtained from the same region in the A layer (Fig. 1(a)), which was relatively less damaged. Compared with the STEM-ABF image obtained from the unirradiated area (Fig. 5(a)), the defect-induced contrast variation in the STEM image can be clearly observed even in this low-damage region, with some areas becoming relatively blacker and brighter in the ABF (Fig. 5(b)) and HAADF image (Fig. 5(c)), respectively. This can be attributed to the lattice disorder induced by the tiny defect clusters [44]. The areas of tiny defect clusters are circumscribed by a dashed line, and the locations of these areas in the ABF and HAADF images agree well.

To clearly display the contrast variation, parts of the areas from Fig. 5(b) and (c) were enlarged and are presented in Fig. 5(e) and (f), respectively; the image in Fig. 5(d) (enlarging from Fig. 5(a)) is provided as a comparison standard. Using Gatan Digital Micrograph software, the measured average (0004) plane spacing from an inverse fast Fourier transform (IFFT) pattern in the unirradiated area is approximately 2.47 Å, as shown in Fig. 5(d), almost the same as the previously reported result of 2.51 Å determined using XRD [45]. However, in the area with contrast change, the lattice plane spacing was increased to approximately 2.72 Å on average. The expansion of the lattice plane might be attributed to the tiny

407 interstitial-type cluster formed in these areas [46]. In addition, the area with

408 contrast variation in the HAADF image marked by a solid line in (Fig. 5(c))

409 was enlarged and is displayed in Fig. 5(f). The difference in image contrast

410 is corroborated by the intensity profiles displayed beneath the

411 corresponding columns, which were obtained using Gatan

412 DigitalMicrograph software across the column along the arrow direction.

413 The intensity of the center columns of this selected area increased. As there

414 was no heavier atom doped into the materials, the increased contrast might

415 arise from the interstitial-type clusters [(47),48)]. The ABF- and

416 HAADF-STEM results for the A layer suggest that most of the tiny defect

417 clusters observed in the A layer should be interstitial-type defects.
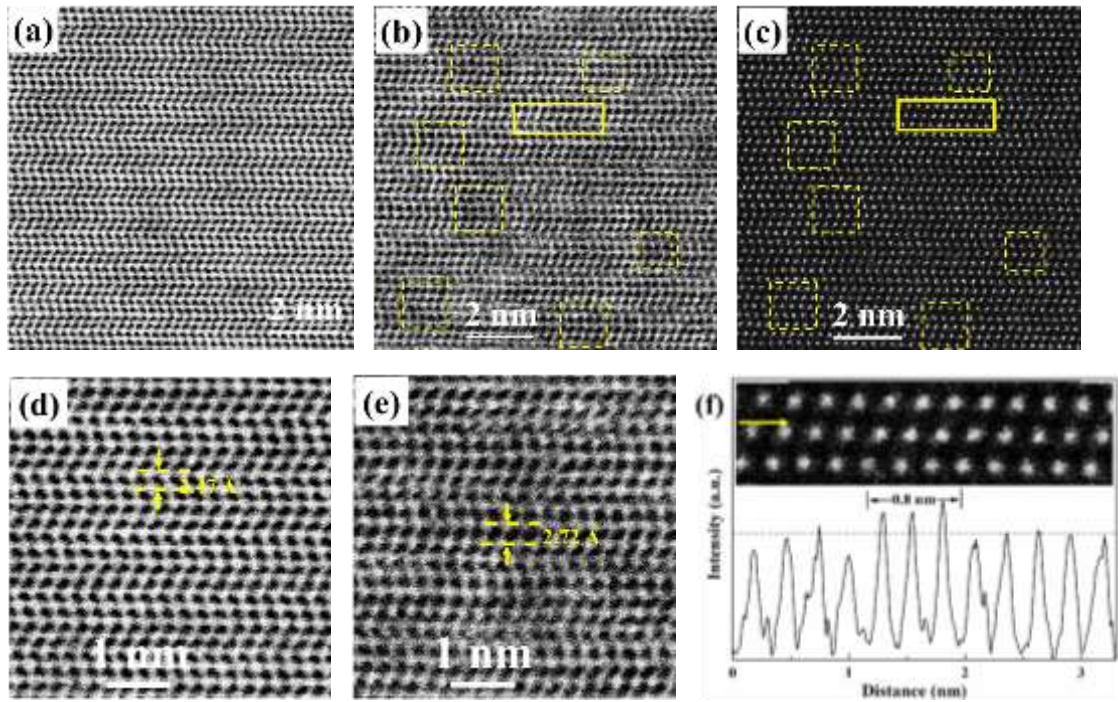
418

419

420 Fig. 5. STEM images obtained from unirradiated area and A layer along the $[11\bar{2}0]$

421 zone axis. (a) ABF image from unirradiated area. (b) ABF image and (c) HAADF image

422 obtained from same region in the A layer. (d) Enlarged image of the area in (a). (e)

Enlarged image of the area in (b). (f) Enlarged image of the area marked by the solid line in (c) and the intensity of each atom column along the arrow direction. The contrast-changed areas are marked by dashed lines and solid lines.

BSDs are usually identified in HR-TEM images by the black image contrast, as observed in Fig. 1(e). Comparing the ABF-STEM image and HR-TEM image in the same area (Fig. S2 in supplementary material), it is apparent that the BSDs also appeared as black contrast in the ABF-STEM image.

Using ABF- and HAADF-STEM, some larger contrast-changed areas circumscribed by dashed lines were observed in the B_1 layer and near the amorphous/crystal interface, as shown in Fig. 6. These contrast-changed areas can be attributed to the BSDs. In addition, the average size of these contrast-changed areas in Fig. 6 is approximately 5 nm, agreeing well with the size of BSDs summarized in Table 1, which also supports their designation as BSDs. The lattice-plane spacing was also expanded in these areas. Moreover, in some areas, such as in Fig. 6(c), which was enlarged from the area in Fig. 6(b) circumscribed by the red solid line, some extra planes of atom columns were observed, as confirmed by the IFFT image of this area (Fig. 6(d)). These extra planes also indicate that most defects formed in the contrast-changed areas should be interstitial type. Therefore, the above results suggest that the BSDs formed in our samples should mainly be interstitial-type clusters, which is consistent with the mobility of interstitials and vacancies in SiC. Bockstedte et al. reported that the

migration energies of vacancies are 3.2–3.6 eV and 3.5–5.2 eV in Si and C [49], respectively, whereas the migration energies of interstitials have been reported to be 1.53 eV in Si and 0.74 eV in C [50]. The Si vacancies in SiC become sufficiently mobile at 800 °C–900 °C [51], and C vacancies may require a higher temperature. It should be pointed out that interstitials are believed to be immobile based on the thermal equilibrium dynamics at room temperature. However, it has also been reported that during the ballistic collision process, the energy deposition from ions to a crystalline could also cause local heating (i.e., an elastic thermal spike) and intense ionization that can lead to localized electronic excitations and local lattice heating (i.e., an inelastic thermal spike). Besides, experimental results have demonstrated that this energy deposition could result in defect formation, diffusion and local structures driven far from equilibrium [52]. Recently, it has also found that the associated defects recovery and diffusion, due to the inelastic thermal spike and localized electronic excitation, are independent of ambient sample temperature [53]. Moreover, molecular dynamics simulation has confirmed the enhanced fission gas diffusion in UO_2 due to the ionization-induced thermal spike [54]. Therefore, the defect clusters (i.e., BSDs) formed in our samples might be attributed to the irradiation-enhanced defect diffusion. As interstitials have a lower migration energy barrier compared with vacancies, they could relatively easily move and combine into clusters in our study. In addition, M. Bockstedte et al. [55] investigated the annealing of vacancies and interstitials in SiC by an ab initio method based on density-functional

theory, which found that the higher mobility of carbon and silicon interstitials compared to the vacancies at lower temperatures drives the formation of interstitial carbon clusters. C. Liu et al. [7] developed a cluster dynamic model by regarding the BSD as an interstitial cluster and proposing additional physical phenomena likely to be present in irradiated SiC. The cluster distributions predicted by their simulations yield an agreement with those measured experimentally, which also supports that BSDs are interstitial type defects.
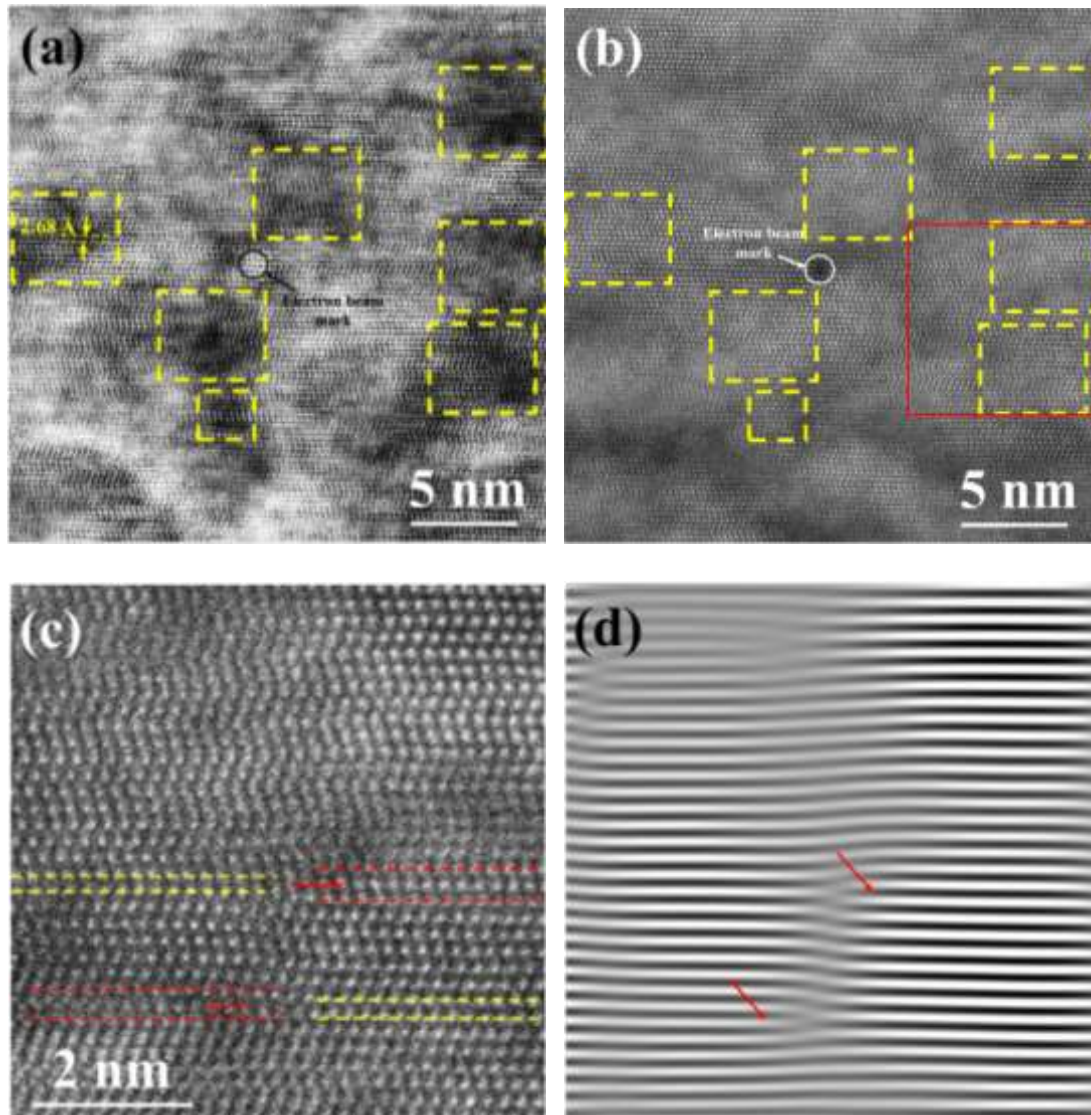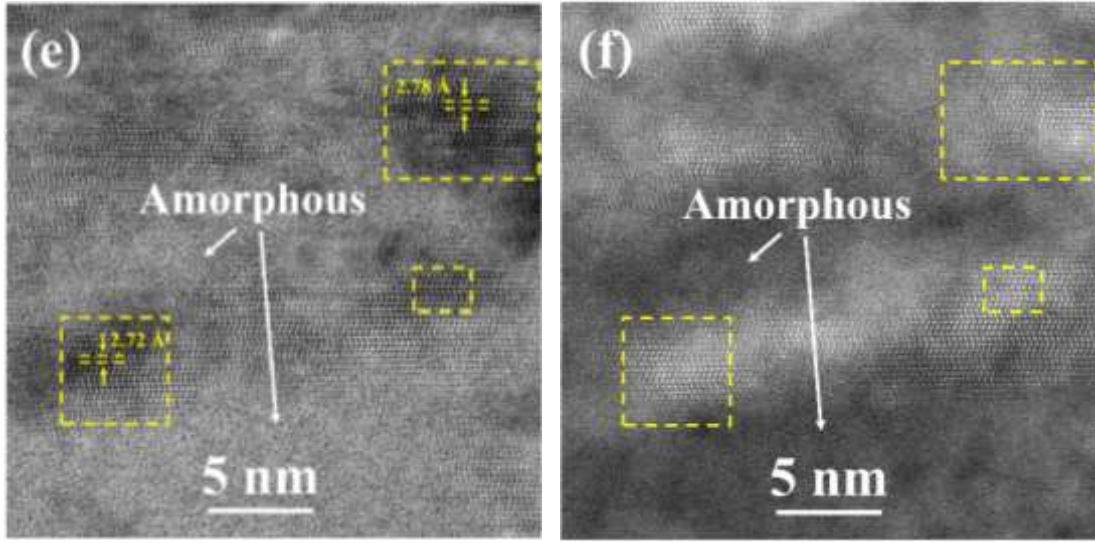
Fig. 6. STEM image obtained from B_1 layer and near the amorphous/crystal interface along the $[11\bar{2}0]$ zone axis. (a, b) were obtained from same region in the B_1 layer: (a) ABF image and (b) HAADF image. (c) is enlarged from the area in (b) circumscribed by the red solid line. (d) Image of inverse fast Fourier transform of (c). (e, f) were obtained from the same region near the amorphous/crystal interface: (e) ABF image and (f) HAADF image. In (a) and (b), a mark was made by an electron beam to confirm the position of each image.

4. Discussion

4.1 Anisotropic defect distribution

The samples in the current study were selected-area ion irradiated such that SiC could freely expand in the Z direction with swelling in the lateral direction (X and Y directions) constrained. These conditions resulted in anisotropic strain or swelling in the sample with a tensile strain in the Z direction and compressive strain in the X and Y directions. The X, Y, and Z directions correspond to lattice orientations of $[11\bar{2}0]$, $[10\bar{1}0]$, and $[0004]$ in these samples, respectively [32].

The anisotropic BSD distribution was determined using conventional TEM, and these defect clusters should mainly be interstitial type in view of the STEM results and defect mobility in SiC. As BSDs correspond to the accumulation of point defects, the formation of more and larger BSDs in the [0004] orientation implies that more interstitial defects were preferentially redistributed in the [0004] orientation compared with in the other two orientations. The defect distribution is correlated to the strain/swelling in the sample. In general, interstitial defects cause the expansion of the lattice around them. The detected defect distribution implies that the tensile strain introduced in the [0004] orientation should be higher than that in the other two orientations. This deduction agrees well with the anisotropic strain condition of our samples with tensile strain in the [0004] orientation and compressive strain in the $[10\bar{1}0]$ and $[11\bar{2}0]$ orientation [32]. Moreover, even though with relative lower number density, the BSDs in the $[10\bar{1}0]$ and $[11\bar{2}0]$ direction are still expected to expand the lattice of the corresponding direction, compressive strain is introduced in these two directions. This implies that more defects with negative volume effect, i.e., vacancy [56] and/or carbon antisite defects (carbon atom occupying the Si-vacancy site, C_{Si}) [4,27,57], than interstitial defects should be introduced in these two directions. It is well known that vacancies are simultaneously introduced into SiC with interstitials; however, the presence of C_{Si} defects remains unclear.

Fig. 7(a) and (b) display the STEM-EELS core-loss spectra of the silicon $L_{2,3}$-edge and carbon K-edge, respectively, acquired from different

26

522　damaged layers. To facilitate identification, the reference spectra of

523　single-crystal silicon and amorphous carbon are also presented in Fig. 7(a)

524　and 7(b), respectively. The core-loss of EELS spectrum could provide the

525　insight into the bonding structure of materials with its peak position and

526　peak shape. For the SiC crystal lattice structure, it is tetrahedral that the

527　carbon atom is surrounded by four silicon atoms, corresponding to the sp^3

528　mode with the bond of C–Si, and this bonding structure shows the $1s \rightarrow \sigma^*$

529　peak at about 290 eV of the core-loss carbon K-edge spectrum, such as the

530　spectrum of "Unirr" in the Fig. 7(b). For amorphous carbon, it shows the

531　graphite like structure that carbon atom is surrounded by three carbon

532　atoms, corresponding to a sp^2 configuration, which shows both π^* (C=C)

533　and σ^* (C–C) peaks at about 283 eV and 295 eV [58,59], respectively, such

534　as the spectrum of "Am. C" in the Fig. 7(b). It is clear that the transition of

535　C-Si bond to C–C and/or C=C bond in the SiC require a displacement of Si

536　atom with C atom, which would result in the formation of C_{Si} (carbon atom

537　occupying the Si-vacancy site), i.e., the appearance of peak at about 283 eV

538　$(1s \rightarrow \pi^*)$ and 295 eV $(1s \rightarrow \sigma^*)$ in the carbon K-edge core-loss EELS

539　spectrum would be evidence of the presence of C_{Si}.

540　　For the core-loss EELS spectra in the He^+ irradiated SiC, the peaks

541　gradually broadened with increasing damage (from the A to C layer) in

542　terms of the Si $L_{2,3}$-edge peak at ~103 eV (Fig. 7(a)) and the carbon K-edge

543　$1s \rightarrow \sigma^*$ peak at about 290 eV, especially for the B1 and C layer, which

544　indicates the damage or decreasing of the C-Si tetrahedral bond structure in

545　SiC. As comparing the "unirr" spectrum with the "A" spectrum in the Fig.

546 (b), it is shown that the left side (280~290 eV) of the σ* peak (290 eV)

547 seems not broadening. However, its right side (290~300 eV) becomes

548 broadened and smoothing, and this energy region just corresponds to the

549 carbon σ* peak (295 eV) of the "Am. C" spectrum. This may suggest the

550 appearance of carbon σ* peak at 295 eV, and also the formation of C–C

551 bond structure and the C_{Si}. With increasing damage, such as the B1 and C

552 layer, the broadening of this peak (290 eV) at the region of 290~300 eV

553 becomes more dominant. Moreover, a 1s→π* shoulder peak (283 eV) was

554 also observed in the spectra acquired from the B1 and C layer, which

555 further confirms the presence of C_{Si} in the selected-area irradiated 4H-SiC.

556 It should be pointed out that the formation of 1s→π* peak (283 eV)

557 indicates the irradiation-induced bonding configuration shifting from sp^3 to

558 sp^2 in SiC, which requires a highly damaged state, such as the formation of

559 defect clusters or amorphization. Thus, it is observed only in the B1 and C

560 layer. The transition of C–Si to C–C (and/or C=C) bond detected in our

561 previous Raman analysis also implies the occurrence of the C_{Si} [32]. In

562 previous works of Kondo et al. [4], an increase in the population of antisite

563 C_{Si} was also observed in Si^{2+}-irradiated SiC fiber, which was implicated as

564 the primary cause for the shrinkage of the irradiated SiC fibers.

565 Considering the negative volume effect of C_{Si} [4,60], the antisite defect of

566 C_{Si} may be dominantly located in ($[11\bar{2}0]$) and ($[10\bar{1}0]$), contributing to

567 the lateral (X- and Y-direction) compressive strain in selected-area

568 ion-irradiated 4H-SiC. Therefore, in the selected-area ion-irradiated

569 4H-SiC, it is likely that interstitial defects are preferentially redistributed in

570 the freely expanding direction (Z, [0004] orientation) with vacancy and/or

571 carbon antisite defects dominantly located in the constrained swelling

572 direction (X and Y, [11$\bar{2}$0] and [10$\bar{1}$0] orientation).
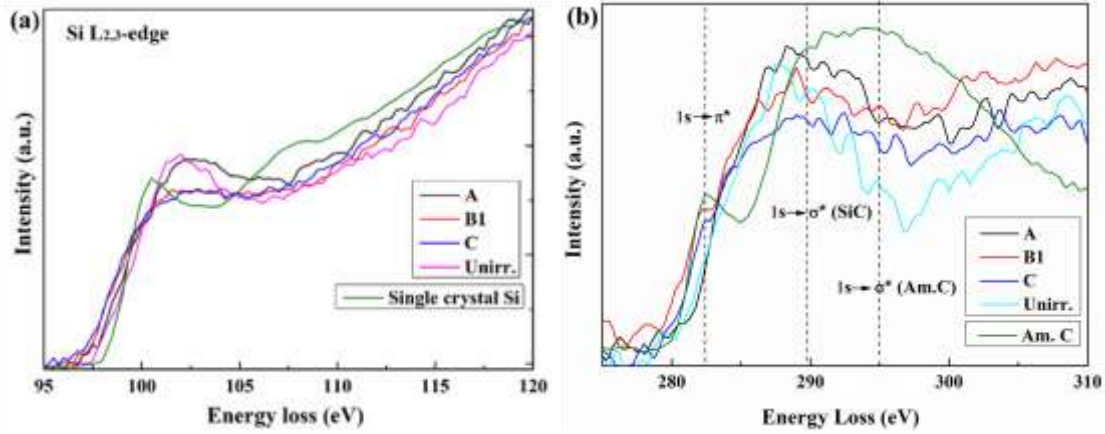

574 Fig. 7 Irradiation-induced change of EELS core-loss spectra: (a) Si L$_{2,3}$-edge spectra

575 and (b) carbon K-edge spectra. The inset letters correspond to the layers marked in Fig.

576 1(a). Reference spectra of single-crystal silicon and amorphous carbon obtained from

577 the Gatan EELS website (https://eels.info/atlas/carbon) are provided for ease of

578 identification.

579

580 4.2 Potential mechanism for anisotropic defect distribution

581   The different number density and size distribution of BSDs (shown in

582 Table 1 and Fig. 4(a)) indicate different nucleation and growth conditions

583 for the different orientations or planes. It is apparent that BSDs in the [0004]

584 orientation have more nucleation sites and a higher growth rate. Defect

585 formation and growth in SiC during ion irradiation mainly arise from the

586 irradiation-induced point defects and their diffusion and combination. Ion

587 irradiation usually introduces nearly the same number of interstitials and

vacancies (Frenkel pairs) in SiC. The anisotropic defect distribution in our sample can mainly be attributed to the different mobilities of interstitials and vacancies, which usually control the defect type and distribution. As the sample was irradiated at room temperature, where interstitial point defects are mobile and vacancies are not, it is likely that some of the interstitials might be redistributed from the $[10\bar{1}0]$ and $[11\bar{2}0]$ orientations to the $[0001]$ orientation to reduce the internal energy because of the habit plane for (0001), resulting in larger and more interstitial-type BSDs in the interplane of $[0004]$.

It has been reported that differential swelling leads to significant stresses [18,24]. Using EBSD, the stress distributions in irradiated and unirradiated areas were measured, as shown in Fig. 8 with (b), (c), and (d) corresponding to the stress in the X ($[11\bar{2}0]$), Y ($[10\bar{1}0]$), and Z ($[0001]$) directions, respectively. It is clear that because of the restriction of swelling, great compressive stress was introduced in both the X and Y directions with an average of -0.94 and -1.15 GPa, respectively; however, little stress arose in the Z direction because of the relaxation of swelling. Moreover, the stress distribution in the other sample with substantially lower fluence of 1×10^{15} cm^{-2} was also measured by EBSD, as shown in Fig. 9. The anisotropic stress distribution was also distinct in this sample with relatively large compressive stress in the X (-0.23 GPa) and Y (-0.36 GPa) directions but little in the Z direction. This result indicates that the compressive stress in the lateral direction begins to accumulate even at the beginning of irradiation. Kondo et al. [61] reported that compressive stress

30

likely inhibits the interstitial-type loop nucleation in planes perpendicular

to the stress axis, resulting in an anisotropic Frank loop development in

ion-irradiated SiC. In Table 1 and Fig. 4(a), the BSDs in the lateral

direction have a lower number density and smaller size. It is likely that the

lateral compressive stress introduced during irradiation inhibits the

nucleation and growth of interstitial defects. This anisotropy of the defect

distribution in selected-area He$^+$-irradiated 4H-SiC can be mainly attributed

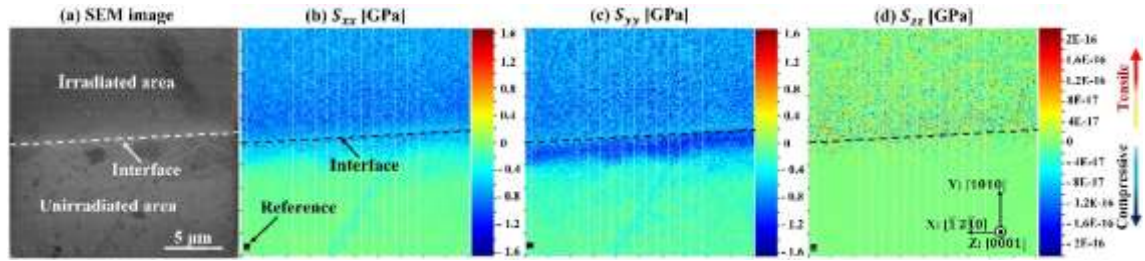to the different stress conditions in the different directions.

Fig. 8. Stress distribution in selected-area He$^+$-irradiated 4H-SiC with fluence of 5×10^{16} cm^{-2}: (a) SEM image and (b)–(d) corresponding stress composition in (b) X, (c) Y, and (d) Z direction. The strain distribution in this region is provided in the supplementary materials of Ref. [32].
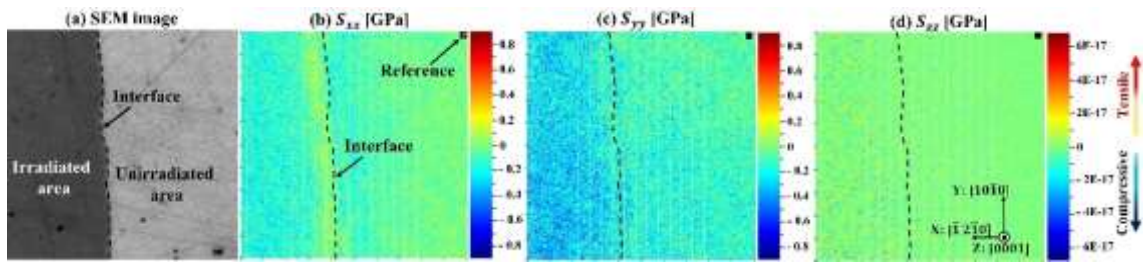

Fig. 9. Stress distribution in selected-area He$^+$ irradiated 4H-SiC with fluence of 1×10^{15} cm^{-2}: (a) SEM image and (b)–(d) corresponding stress composition in (b) X, (c) Y, and (d) Z direction.

630 4.3 Defect distribution in non-selected-area He$^+$-irradiated 4H-SiC

631   For comparison, a non-selected-area He$^+$-irradiated 4H-SiC sample was

632 prepared using the same fluence of 5×10^{16} cm^{-2}. The defect distribution in

633 this sample is shown in Fig. 10. The observed difference in the different

634 directions in this sample appears to be smaller than that in the selected-area

635 irradiated 4H-SiC (Fig. 2). The calculated average size and number density

636 of the BSDs are summarized in Table 1. The BSDs in different directions

637 were similar in average size with a higher number density in the [0004]

638 direction. The defect distribution remained slightly anisotropic in this

639 sample. However, its anisotropy was substantially smaller than that in the

640 selected-area irradiated samples in terms of the average size and number

641 density of BSDs. This result is supported by the similar defect size

642 distributions in the different directions in Fig. 4(b). Without constraint in

643 the lateral direction, the compressive stress introduced in the

644 non-selected-area irradiated sample should be lower than that in the

645 selected-area irradiated sample. The relatively lower anisotropy of the

646 defect distribution in the non-selected-area He$^+$-irradiated 4H-SiC indicates

647 the restraining effects of the compressive stress on the formation of

648 interstitial defects.

649   Although relatively smaller, an anisotropic defect distribution remained

650 in this non-selected-area irradiated sample. It has been reported that

651 compressive stress would also be introduced in the lateral direction in

652 ion-irradiated SiC, which is attributed to the constraint against lateral

653 expansion owing to the shallow thickness of the irradiated layer compared

with the sample thickness in contrast to the free expansion allowed along the surface normal [61]. Hence, the anisotropic defect distribution in the non-selected-area ion-irradiated sample may also be attributed to the compressive stress introduced in the lateral direction.
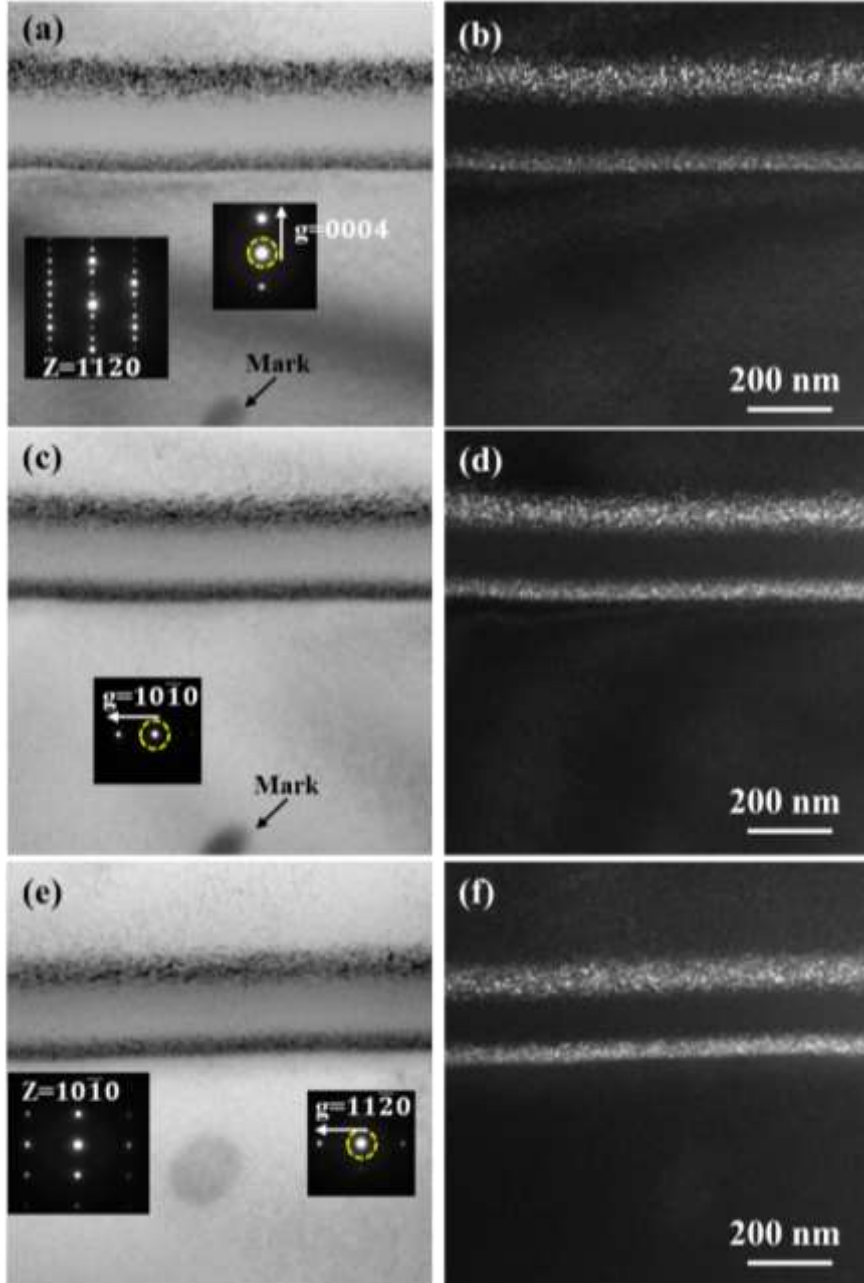

Fig. 10 TEM images of BSDs in non-selected-area He$^+$-irradiated 4H-SiC with fluence of 5×10^{16} cm^{-2}. (a), (c), and (e) are two-beam bright-field images with g=0004, $10\bar{1}0$,

661 and $11\bar{2}0$, respectively, and (b), (d) and (f) are their corresponding weak-beam

662 dark-field images with g/3g. (a–d) were obtained from the same area, and (e, f) were

663 obtained from another area.

664

665 4.4 Defect distribution in electron-irradiated thin-film 4H-SiC

666   It has been reported that the introduction of compressive stress in the

667 lateral direction may even be possible in non-selected-area ion-irradiated

668 bulk samples because of the constraint against lateral expansion [61]. For

669 comparison, the electron irradiation was performed on a TEM-foil sample

670 of 4H-SiC at room temperature. Before irradiation, the samples were

671 annealed at 600 °C for 30 min to remove any potential internal stress.

672 During irradiation, the electron beam was parallel to the $[11\bar{2}0]$ zone axis.

673 Hence, compared with the He$^+$-irradiated bulk sample, there were two main

674 differences in terms of the stress condition that should be noted in the

675 electron-irradiated sample. One is that the lateral stress in the

676 electron-irradiated area should be relatively lower because of the relatively

677 thinner electron-irradiated sample, though electron irradiation is also a type

678 of selected-area irradiation. The other is that the [0004] and $[10\bar{1}0]$

679 orientations should have a similar stress as both are lateral directions as the

680 electron beam was along the $[11\bar{2}0]$ direction. Therefore, the different

681 stress states in the [0004] and $[10\bar{1}0]$ orientations in the ion-irradiated

682 sample could be neglected in this electron-irradiated sample.

683   The defect distributions in the centers of the electron-irradiated areas are

684 shown in Fig. 11, and the counted average size and number density of

685 BSDs are summarized in Table 1. The size distribution of BSDs is shown in

686 Fig. 4(c). The BSDs formed under electron irradiation were larger in

687 average size and lower in number density than those under ion irradiation.

688 This may be attributed to a larger flux density of electron beam irradiation

689 $(1.2\times10^{24}$ e·m^{-2}·s$^{-1})$ compared with the ion irradiation $(6.2\times10^{16}$ He·m^{-2}·s$^{-1})$

690 and also the surface effects of the TEM-foil sample. From the average size,

691 number density, and size distribution of BSDs in the $[10\bar{1}0]$ and $[0004]$

692 orientations, the defect distribution in electron-irradiated 4H-SiC also

693 appears to be anisotropic. However, the ratios of the average size and

694 number density between the $[0004]$ and $[10\bar{1}0]$ orientation were 1.15

695 (7.1/6.2) and 1.52 (1.1/0.72) (Table 1), respectively, in the

696 electron-irradiated sample, which are substantially smaller than the ratios

697 of 1.41 (5.5/3.9) and 2.64 (2.9/1.1), respectively, in the selected-area

698 He$^+$-ion-irradiated sample. Therefore, it is apparent that the anisotropy of

699 the defect distribution in the selected-area He$^+$-irradiated sample was

700 enhanced, which can be primarily attributed to the compressive stress

701 introduced in the lateral direction during irradiation.

702 It should be noted that the different irradiation conditions for ion

703 irradiation and electron irradiation, including the different dose rates,

704 different irradiation particle energies, and the cascade effect, might

705 contribute to the different defect evolution. In particular, interstitial and

706 vacancy atoms might annihilate on the surface of the thin sample used in

707 the electron irradiation, which would greatly affect the defect distribution

708 in the sample. However, the above cases should have a similar effect on the

defect distribution for the [0004] and [10$\bar{1}$0] directions, and they might not greatly change the anisotropy of the defect distribution between the [0004] and [10$\bar{1}$0] directions. Hence, the great difference in the anisotropy of the defect distribution between the selected-area ion irradiation and electron irradiation can be mainly attributed to the compressive stress introduced during ion irradiation.

Similar to the non-selected-area He$^+$-irradiated sample, anisotropic defect distribution was also somewhat introduced in the electron-irradiated foil sample. However, the stress effect on the anisotropy should be quite low in the electron-irradiated sample, as discussed above. Stress should not be the primary cause for the anisotropy between the [0004] and [10$\bar{1}$0] directions in the electron-irradiated sample. Hence, the anisotropic defect distribution in the non-selected-area ion-irradiated sample and electron-irradiated sample might not only be attributed to the stress, and some other potential mechanisms might exist [27,31,62]. Anisotropic swelling is also observed in the reported result that a shrinkage of the a-axis is formed at extremely low doses of 1.26×10^{-3} dpa in H$^+$-irradiated 6H-SiC with an expansion in the c-axis, which could be associated with irradiation-induced vacancies in the a-axis [27]. Therefore, the initial anisotropic distribution of defects in ion-irradiated α-SiC might be attributed to the intrinsic property of α-SiC, such as the larger parameter of the c-axis than that of a-axis. The interstitial atoms would expand the lattice, and the local crystal structure around a vacancy could contract. When a C or Si atom is removed from the lattice site in a unit cell of α-SiC, a local

36

733   lattice strain is induced, and a repositioning of the surrounding atoms

734   occurs to minimize the internal energy. The anisotropy of defect

735   distribution, i.e., the interstitial atoms redistributed into c-axis (which is

736   larger in plane space) and vacancies and/or C_{Si} located into the a-axis,

737   seemly better to minimize the strain and disorder induced by irradiation.

738   This interpretation agreed with the distribution of interstitial type defect of

739   helium platelet, which has been reported to preferentially form in the c-axis

740   [63]. In addition, the modeling results showed that the activation barrier for

741   a migration of carbon interstitials in the 4H–SiC is the lowest along the

742   c-axis ($[000\bar{1}]$) compared with the $[11\bar{2}0]$ and $[10\bar{1}0]$ [64], which also

743   agrees well with the defect distribution in our study. This suggests that the

744   different migration energy for a defect along the different axes in the α–SiC

745   would also contribute to the anisotropic defect distribution and the

746   anisotropic swelling. As the compressive stress is introduced into the a-axis,

747   i.e., selected-area He$^+$-irradiated 4H-SiC, a higher anisotropic defect

748   distribution is observed, which shows an enhanced tendency of defect

749   repositioning discussed above. The compressive stress would compact the

750   plane space in the a-axis, which seemly inhibits the interstitial type defect

751   formation in this direction and enhances the anisotropic defect distribution

752   in the He$^+$ irradiated 4H-SiC. In addition, it has been reported that the

753   irradiation-induced tensile strain would cause the drift of interstitial atoms,

754   resulting in a higher tensile strain [65]. Considering the strain condition in

755   the selected-area He$^+$-ion-irradiated 4H-SiC that tensile strain in the [0004]

756   orientation and compressive strain in $[10\bar{1}0]$ and $[11\bar{2}0]$, it is possible

37

757 that this strain condition would affect defect drift and enhance the
758 anisotropic defect distribution, which would in turn result in higher
759 anisotropic swelling. Therefore, the observed anisotropic defect distribution
760 in the selected-area He⁺-irradiated 4H-SiC should be attributed to the
761 integrated effects, including both the intrinsic properties of α-SiC and the
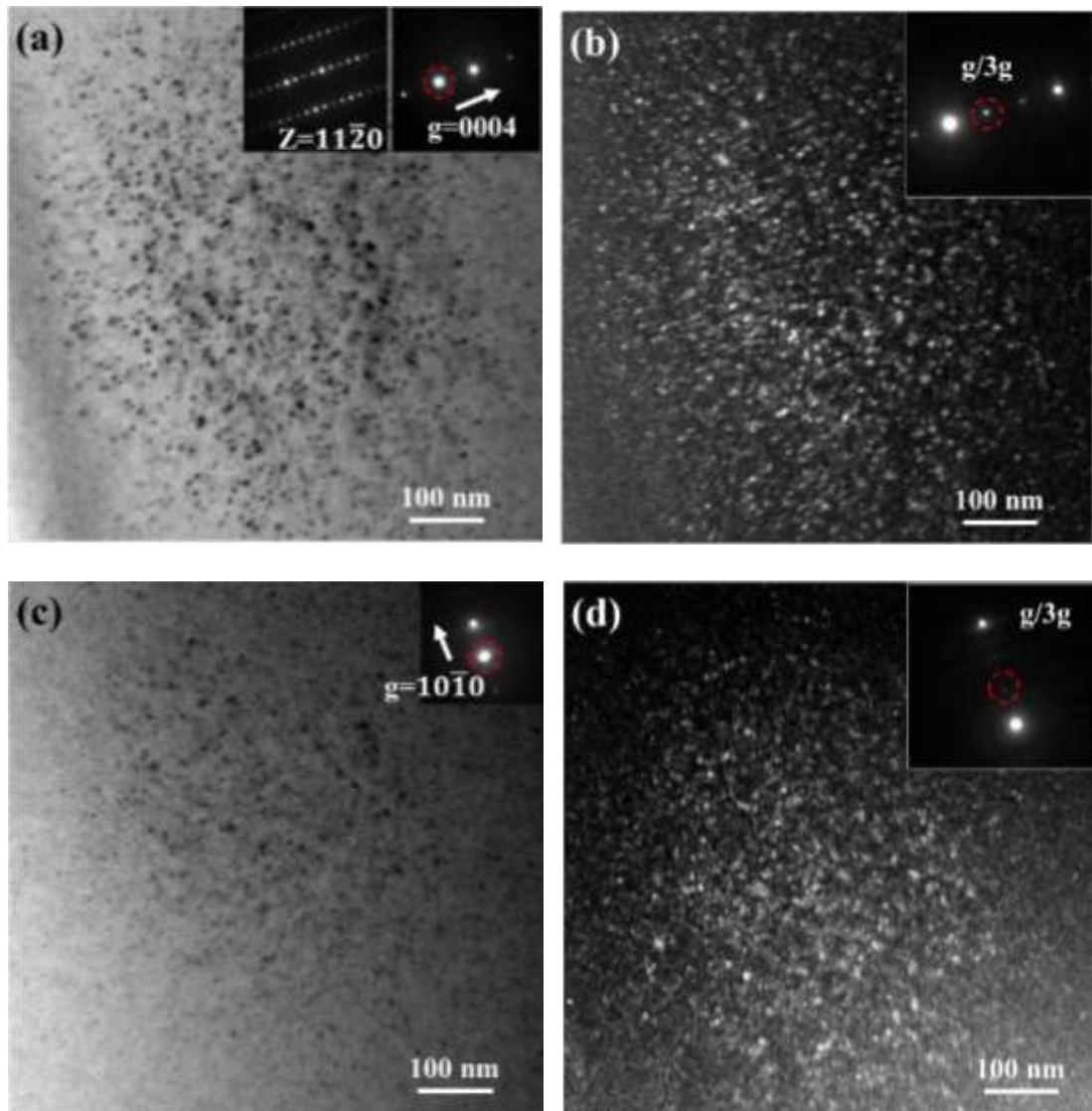762 compressive stress in a-axis.

763

764

765 Fig. 11. TEM images of BSD distribution in the center of electron irradiation area of
766 electron-irradiated 4H-SiC: (a, b) g=0004 and (c, d) g=10$\bar{1}$0, with (a, c) bright-field

767 images and (b, d) weak-beam dark-field images, g/3g. These images were obtained from

768 the same area.

769

5. Summary

771 Using TEM techniques, the defect distribution in selected-area

772 He$^+$-irradiated 4H-SiC with irradiation-induced anisotropic swelling was

773 explored, and anisotropy of the defect distribution was observed. Interstitial

774 defects were preferentially redistributed to the freely expanding direction

775 (Z direction, [0004] orientation) with negative volume defects dominantly

776 located in the constrained swelling directions (X and Y directions,

777 [11$\bar{2}$0] and [10$\bar{1}$0] orientations). This anisotropy of the defect

778 distribution was substantially larger than that in non-selected-area

779 He$^+$-irradiated 4H-SiC and electron-irradiated thin-foil 4H-SiC.

780 Compressive stress was introduced in the lateral direction (X and Y

781 directions, [10$\bar{1}$0] and [11$\bar{2}$0] orientations), with little introduced in the

782 surface normal direction (Z direction, [0004] orientation) in the

783 selected-area He$^+$-irradiated 4H-SiC because of the constraint against

784 lateral expansion, and these compressive stresses were introduced at the

785 beginning of ion irradiation. The compressive stress introduced during

786 irradiation was speculated to inhibit the formation of interstitial defects,

787 enhancing the anisotropic defect distribution in the selected-area

788 ion-irradiated 4H-SiC.

789

References

[1] Y. Zhang, R. Sachan, O. H. Pakarinen, M. F. Chisholm, P. Liu, H. Xue, W. J. Weber, Ionization-induced annealing of pre-existing defects in silicon carbide, Nat. Commun. 6, 8049 (2015).

[2] L. Nuckols, M. L. Crespillo, C. Xu, E. Zarkadoula, Y. Zhang, W. J. Weber, Coupled effects of electronic and nuclear energy deposition on damage accumulation in ion-irradiated SiC, Acta Mater. 199 (2020) 96–106.

[3] N. Daghbouj, B. S. Li, M. Callisti, H. S. Sen, J. Lin, X. Ou, M. Karlik, T. Polcar, The structural evolution of light-ion implanted 6H-SiC single crystal: Comparison of the effect of helium and hydrogen, Acta Mater. 188 (2020) 609-622.

[4] S. Kondo, T. Hinoki, M. Nonaka, K. Ozawa, Irradiation-induced shrinkage of highly crystalline SiC fibers, Acta Materialia 83 (2015) 1–9.

[5] N. G. Wright, A. B. Horsfall, K. Vassilevski, Prospects for SiC electronics and sensors, Mater. Today 11 (2008).

[6] M. Li, X. Zhou, H. Yang, S. Du, Q. Huang, The critical issues of SiC materials for future nuclear systems, Scr. Mater. 143 (2018) 149–153.

[7] C. Liu, L. He, Y. Zhai, P. M. Voyles, K. Sridharan, D. Morgan, I. Szlufarska, Evolution of small defect clusters in ion irradiated 3C-SiC: Combined cluster dynamics modeling and experimental study, Acta Mater. 125 (2019) 377–389.

[8] Yutai Katoh, Sosuke Kondo, Lance L. Snead, Microstructures of beta-silicon carbide after irradiation creep deformation at elevated temperatures, J. Nucl. Materl. 382 (2008) 170–175.

[9] G.S. Was, Z. Jiao, E. Getto, K. Sun, A.M. Monterrosa, S.A. Maloy, O. Anderoglu, B.H. Sencerc, M. Hackett, Emulation of reactor irradiation damage using ion beams, Scrip. Mater. 88 (2014) 33–36.

[10] Y. Katoh, L. L. Snead, I. Szlufarska, W. J. Weber, Radiation effects in SiC for nuclear structural applications, Cur. Opin. Sol. State Mater. Sci. 16 (2012)143–152.

836 [11] N. Daghbouj, B.S. Li, M. Callisti, H.S. Sen, M. Karlik, T. Polcar,

837 Microstructural evolution of helium-irradiated 6H–SiC subjected to

838 different irradiation conditions and annealing temperatures: A multiple

839 characterization study, Acta Mater. 181 (2019) 160–172.

840 [12] S. Leclerc, A. Declémy, M. F. Beaufort, C. Tromas, J. F. Barbot,

841 Swelling of SiC under helium implantation, J. Appl. Phys. 98 (2005)

842 113506.

843 [13] S. Leclerc, M.F. Beaufort, A. Declémy, J.F. Barbot, Evolution of

844 defects upon annealing in He-implanted 4 H-SiC, Appl. Phys. Lett. 93

845 (2008) 122101.

846 [14] A. Debelle, L. Thome, D. Dompoint, A. Boulle, F. Garrido, J Jagielski,

847 D. Chaussende, Characterization and modelling of the ion-irradiation

848 induced disorder in 6H-SiC and 3C-SiC single crystals, J. Phys. D: Appl.

849 Phys. 43 (2010) 455408.

850 [15] F.W. Clinard, Jr., W. Dienst, E.H. Farnum, Issues related to mechanical

851 properties of neutron-irradiated ceramics, J. Nucl. Materl. 212-215 (1994)

852 1075–1080.

853 [16] I.T. Yano T, Swelling and microstructure of AlN irradiated in a fast

854 reactor, J. Nucl. Materl. 203 (1993) 249–254.

855 [17] T. Yano, M. Akiyoshi, K. Ichikawa, Y. Tachi, T. Iseki, Physical

856 property change of heavily neutron-irradiated Si3N4 and SiC by thermal

857 annealing, J. Nucl. Materl. 289 (2001) 102.

[18] C.A.C. Silva, C. Shih, T. Koyanagi, Y. Katoh, S. J. Zinkle, Anisotropic swelling and microcracking of neutron irradiated Ti3AlC2–Ti5Al2C3 materials, Scr. Mater. 114 (2016) 74–78.

[19] J.C. Nappé, C. Maurice, Ph. Grosseau, F. Audubert, L. Thomé, B. Guilhot, M. Beauvy, M. Benabdesselam, Microstructural changes induced by low energy heavy ion irradiation in titanium silicon carbide, J. European Ceram. Soc. 31 (2011) 1503–1511.

[20] Z. Li, R. C. Bradt, Thermal expansion of the hexagonal (4H) polytype of SiC, J. Appl. Phys. 60 (1986) 612.

[21] H. Kroncke, S. Figge, B.M. Epelbaum, D. Hommel, Determination of the temperature dependent thermal expansion coefficients of bulk AlN by HRXRD, ACTA Phys. Polon. A, 114 (2008) 1193-1200.

[22] T. H. Scabarozi, S. Amini, O. Leaffer, Thermal expansion of select phases measured by high temperature x-ray diffraction and dilatometry, J. Appl. Phys. 105 (2009) 013543.

[23] S. Kondo, T. Koyanagi, T. Hinoki, Irradiation creep of 3C–SiC and microstructural understanding of the underlying mechanisms, J. Nucl. Materl. 448 (2014) 487–496.

[24] S. Smolentsev, N.B. Morley, M. Abdou, Magnetohydrodynamic and thermal issues of the SiC_f/SiC flow channel insert, Fusion Sci. Technol. 50 (2006) 107–119.

[25] L.L. Snead, Y. Katoh, T. Koyanagi, K. Terrani, E.D. Specht, Dimensional isotropy of 6H and 3C SiC under neutron irradiation, J. Nucl. Materl. 471 (2016) 92–96.

882 [26] Y. Lin, C. Ho, W. Chuang, C. Ku, J. Kai, Swelling of ion-irradiated

883 3C–SiC characterized by synchrotron radiation based XRD and TEM, J.

884 Nucl. Materl. 455 (2014) 292–296.

885 [27] W. Jiang, P. Nachimuthu, W. J. Weber, L. Ginzbursky, Variation in

886 lattice parameters of 6H-SiC irradiated to extremely low doses, Appl. Phys.

887 Lett. 91 (2007) 091918.

888 [28] Y. Zhang, W. J. Weber, W. Jiang, C. M. Wang, V. Shutthanandan, A.

889 Hallen, Effects of implantation temperature on damage accumulation in

890 Al-implanted 4H–SiC, J. Appl. Phys. 95 (2004) 4012.

891 [29] B. Tyburska-Püschel, Y. Zhai, L. He, C. Liu, A. Boulle, P. M.

892 Voyles, I. Szlufarska, K. Sridharan, Size distribution of black spot defects

893 and their contribution to swelling in irradiated SiC, J. Nucl. Materl. 476

894 (2016) 132–139.

895 [30] Y. Zhang, F. Gao, W. Jiang, D.E. McCready, W.J. Weber, Damage

896 accumulation and defect relaxation in 4H-SiC, Phys. Rev. B 70 (2004)

897 125203.

898 [31] S. Kondo, C. M. Parish, T. Koyanagi, Y. Katoh, Equilibrium shapes

899 and surface selection of nanostructures in 6H-SiC, Appl. Phys. Lett. 110

900 (2017) 142106.

901 [32] S. Yang, S. Tokunaga, M. Kondo, Y. Nakagawa, T. Shibayama,

902 Non-destructive evaluation of the strain distribution in selected area He+

903 ion irradiated 4H-SiC, Appl. Surf. Sci. 500 (2020).

904 [33] R. Devanathan, T. Diaz de la Rubia, W.J. Weber, Displacement

905 threshold energies in b-SiC, J. Nucl. Materl. 253 (1998) 47–52.

[34] S. Yang, Y. Nakagawa, M. Kondo, T. Shibayama, electron energy-loss spectroscopic evaluation of depth-dependent swelling of He+ ion-irradiated 4H-SiC correlated with defect type, J. Appl. Phys. 127 (2020) 175106.

[35] K. Kamitani, M. Grimsditch, J.C Nipko, C.K. Loong, M. Okada, I. Kimura, The elastic constants of silicon carbide: A Brillouin-scattering study of 4H and 6H SiC single crystals, J. Appl. Phys. 82 (1997) 3152.

[36] B.S. Li, C. Zhang, H.P. Liu, L.J. Xu, X. Wang, Z. Yang, F.F. Ge, W. Gao, T.L. Shen, Microstructural and elemental evolution of polycrystalline α-SiC irradiated with ultra-high-fluence helium ions before and after annealing, Fus. Eng. Des. 154 (2020) 111511.

[37] Y. Katoh, N. Hashimoto, S. Kondo, L.L. Snead, A. Kohyama, Microstructural development in cubic silicon carbide during irradiation at elevated temperatures, J. Nucl. Materl. 351 (2006) 228–240.

[38] C.B. Carter, D.B. Williams, Transmission electron microscopy: a text book for materials science, Springer: New York, 1996.

[39] S. Sandlobes, M. Friak, S. Zaefferer, A. Dick, S. Yi, D. Letzig, Z. Pei, L.F. Zhu, J. Neugebauer, D. Raabe, The relation between ductility and stacking fault energies in Mg and Mg–Y alloys, Acta Mater. 60 (2012) 3011–3021.

[40] H. Zhang, Zhongwen Yao, G. Morin, M. Griffiths, TEM characterization of in-reactor neutron irradiated CANDU spacer material Inconel X-750, J. Nucl. Materl. 451 (2014) 88–96.

[41] S. Sandlöbes, M. Friák, J. Neugebauer, D. Raabe, Basal and non-basal dislocation slip in Mg-Y, Mater. Sci. Eng. A 576 (2013) 61–68.

930 [42] Y. Lin, L. Chen, C. Hsieh, A. Hu, S. Lo, F. Chen, J. Kai, Atomic

931 structure of nano voids in irradiated 3C-SiC, J. Nucl. Materl. 498 (2018)

932 71–75.

933 [43] Eiji Okunishi, Hidetaka Sawada, Yukihito Kondo, Experimental study

934 of annular bright field (ABF) imaging using aberration-corrected scanning

935 transmission electron microscopy (STEM), Micron 43 (2012) 538–544.

936 [44] J. Q. Liu, M. Skowronski, C. Hallin, R. Soderholm, H. Lendenmann,

937 Structure of recombination-induced stacking faults in high-voltage SiC p- n

938 junctions, Appl. Phys. Lett. 80 (2002) 749–751.

939 [45] A. L. Hannam, P. T. B. Shaffer, Revised X-ray Diffraction Line

940 Intensities for Silicon Carbide Polytypes, J. Appl. Cryst. 2 (1969) 45.

941 [46] J. Li, Z. Wang, C. Chen, S. Huang, Atomic-scale observation of

942 migration and coalescence of Au nanoclusters on YSZ surface by

943 aberration-corrected STEM, Sci. Rep. 4 (2014) 5521.

944 [47] K. Watanabe, E. Asano, T. Yamazaki, Y. Kikuchi, I. Hashimoto,

945 Symmetries in BF and HAADF STEM image calculations,

946 Ultramicroscopy 102 (2004) 13–21.

947 [48] S. J. Pennycook, D. E. Jesson, High-resolution Z-contrast imaging of

948 crystals, Ultramicroscopy 37 (1991) 14–38.

949 [49] M. Bockstedte, A. Mattausch, O. Pankratov, Ab initio study of the

950 migration of intrinsic defects in 3C-SiC, Phys. Rev. B 68 (2003) 205201.

951 [50] F. Gao, W. J. Weber, Recovery of close Frenkel pairs produced by low

952 energy recoils in SiC, J. Appl. Phys. 94 (2003) 4348–4356.

[51] E. Oliviero, M.F. Beaufort, J.F. Barbot, A. van Veen, A.V. Fedorov, Helium implantation defects in SiC: A thermal helium desorption spectrometry investigation, J. Appl. Phys. 93 (2003) 231–238.

[52] Y. W. Zhang, W. J. Weber, Ion irradiation and modification: The role of coupled electronic and nuclear energy dissipation and subsequent nonequilibrium processes in materials, Appl. Phys. Rev. 7 (2020) 041307.

[53] G. Velişa, E. Wendler, S. Zhao, et al. Delayed damage accumulation by athermal suppression of defect production in concentrated solid solution alloys, Mater. Res. Lett. 6 (2018) 136–141.

[54] M.W.D. Cooper, C.R. Stanek, J.A. et al. Simulation of radiation driven fission gas diffusion in UO2, ThO2and PuO2, J. Nucl. Mater. 481(2016) 125.

[55] M. Bockstedte, A.r Mattausch, O. Pankratov, Ab initio study of the annealing of vacancies and interstitials in cubic SiC: Vacancy-interstitial recombination and aggregation of carbon interstitials, Phys. Rev. B 69 (2004) 235202.

[56] P. H. Dederiches, C. Lehmann, H. R. Schober, A. Scholz, R. Zeller, lattice theory of point defects, J. Nucl. Mater. 69-70 (1978) 176-199.

[57] J. Li, L. Porter, S. Yip, Atomistic modeling of finite-temperature properties of crystalline b-SiC II. Thermal conductivity and effects of point defects, J. Nucl. Materl. 255 (1998) 139–152.

[58] L. Ponsonnet, C. Donnet, K. Varlot, J.M. Martin, A. Grill, V. Patel, EELS analysis of hydrogenated diamond-like carbon films, Thin Solid Films, 319 1998 97–100.

[59] S. Wakeland, R. Martinez, J. K. Grey, C. C. Luhrs, Production of graphene from graphite oxide using urea as expansion–reduction agent, Carbon, 48 (2010) 3463–3470.

[60] P.G. Baranov, I.V. Llyin, A.A. Soltamova, E.N. Mokhov, Identification of the carbon antisite in SiC: EPR of ^{13}C enriched crystals, Phys. Rev. B 77 (2008) 085120.

[61] S. Kondo, A. Kohyama, T. Hinoki, Anisotropic evolution of Frank loops in ion-irradiated silicon carbide, J. Nucl. Materl. 367-370 (2007) 764–768.

[62] W. Jiang, W.J. Weber, Anisotropy of disorder accumulation and recovery in 6H–SiC irradiated with Au^{2+} ions at 140 K, J. Nucl. Materl. 389 (2009) 332–335.

[63] R. W. Harrison, S.Ebert, J. A. Hinks, S.E. Donnelly, Damage microstructure evolution of helium ion irradiated SiC under fusion relevant temperatures, J. Eur. Ceram. Soc. 38 (2018) 3718-3726.

[64] E. Rauls, T.E.M. Staab, Z. Hajnal, Th. Frauenheim, Interstitial-based vacancy annealing in 4H–SiC, Physica B 308–310 (2001) 645–648.

[65] S. Leclerc, M.F. Beaufort, A. Declémy, J.F. Barbot, Strain-induced drift of interstitial atoms in SiC implanted with helium ions at elevated temperature, J. Nucl. Mater. 397 (2010) 132–134.